Sputter-engineering a first-order magnetic phase transition in sub-15-nm-thick single-crystal FeRh films

L. Benito,[1,*] L. Clark,[2,†] T. P. Almeida,[2,‡] T. A. Moore,[1]
D. McGrouther,[2] S. McVitie,[2] and C. H. Marrows[1,§]

[1]*School of Physics and Astronomy, University of Leeds, Leeds LS2 9JT, United Kingdom*

[2]*SUPA, School of Physics and Astronomy, University of Glasgow, Glasgow G12 8QQ, United Kingdom*

(Dated: October 9, 2020)

Abstract

Equiatomic FeRh alloys undergo a fascinating first-order metamagnetic phase transition (FOMPT) just above room temperature, which has attracted reinvigorated interest for applications in spintronics. Until now, all attempts to grow nanothin FeRh alloy films have consistently shown that FeRh layers tend to grow in the Volmer-Weber growth mode. Here we show that sputter-grown sub-15-nm-thick FeRh alloy films deposited at low sputter-gas pressure, typically ~ 0.1 Pa, onto (001)-oriented MgO substrates, grow in a peening-induced Frank-van der Merwe growth mode for FeRh film thicknesses above 5 nm, circumventing this major drawback. The bombardment of high-energy sputtered atoms, the atom-peening effect, induces a re-balancing between adsorbate-surface and adsorbate-adsorbate interactions, leading to the formation of a smooth continuous nanothin FeRh film. Chemical order in the films increases with the FeRh thickness, t_{FeRh}, and varies monotonically from 0.75 up to 0.9. Specular x-ray diffraction scans around Bragg peaks show Pendellösung fringes for films with $t_{\mathrm{FeRh}} \geq 5.2$ nm, which reflects in smooth well-ordered densified single-crystal FeRh layers. The nanothin film's roughness varies from 0.6 down to about 0.1 nm as t_{FeRh} increases, and scales linearly with the integral breadth of the rocking curve, proving its microstructured origin. Magnetometry shows that the FOMPT in the nanothin films is qualitatively similar to that of the bulk alloy, except for the thinnest film of 3.7 nm.

* Email:luisp.benito@googlemail.com

† Present address: Department of Materials, University of Oxford, Parks Road, OX1 3PH Oxford, United Kingdom

‡ Present address: CEA, LETI, Minatec Campus, F-38054 Grenoble, France

§ Email:c.h.marrows@leeds.ac.uk

I. INTRODUCTION

First-order phase transitions typically entail abrupt changes in a material's properties [1], which potentially open up new opportunities for tailoring functional devices[2]. FeRh alloys belong to a unique class of technologically sought-after materials, as they possess a fascinating first-order metamagnetic phase transition (FOMPT) originally discovered by Fallot in 1937, while conducting studies on Fe-X (X=Ru [3], Ir [4] and Rh [5]) intermetallic alloys. However, it was later on that Kouvel *et al.* [6], showed that the FOMPT in FeRh alloy can be observed if it is heated up above room temperature. In particular, Fe_xRh_{1-x} alloys close to equiatomic compositions ($48 \leq x \leq 56$ at% Fe) form a B2 ordered CsCl-type crystallographic structure and undergo an intriguing multi-stimuli tuned first-order magnetic phase transition [6]. At low temperature, FeRh adopts an anisotropic collinear type-II [7] antiferromagnetic (AF) phase, where nearest-neighbour Fe sites ordered antiferromagnetically within (001)-planes and ferromagnetically within (111)-planes, transforming to a weakly anisotropic ferromagnetic (F) phase at around about $T \sim 370$ K, which shows the usual thermal hysteresis of a first-order transition. On cooling, the FOMPT in FeRh alloys is accompanied by a massive decrease in volume [8] of $\sim 1\%$ and by large changes in its fundamental physical properties, including for instance a giant magnetoresistance [9] ($\Delta R/R \sim 50\%$) and a giant magnetostriction [8] ($\sim 0.82\%$).

Interestingly for applications, the FOMPT in FeRh alloys shows a wide tunability by a variety of stimuli [10], *e.g.* magnetic field, strain, or chemical doping, among others. Building on such rich phenomena, novel power-efficient spintronics concepts have been recently demonstrated, *e.g.* a robust AF-based memory resistor [11], a voltage-controlled hybrid storage memory [12] device and an exchange-spring coupled heterostructure [13] for near-future heat-assisted magnetic recording technology [14]. However, in order to develop real-world spintronic device prototypes based on active FeRh layers, smoother fully functional thinner FeRh layers will be much needed, typically below 15 nm. Nowadays, conventional physical vapor deposition approaches to growing nanothin FeRh alloy layers are far away from meeting these stringent requirements.

In this Rapid Communication, we show that, in sharp contrast to previous attempts in which nanothin FeRh alloy films were shown to grow in the Volmer-Weber growth mode [15–19], smooth chemically well-ordered single-crystal fully functional nanothin FeRh alloy

films can be synthesized if proper dc-magnetron sputtering deposition parameters are chosen. In particular, we demonstrate that sputter-grown sub-15 nm thick FeRh alloy films deposited at an Ar pressure of about 0.1 Pa onto (001)-oriented MgO substrates grow in an induced Frank-van der Merwe growth mode for t_{FeRh}>5 nm, as consequence of the *atom-peening* [20] effect, *i.e.* the bombardment by highly energetic sputtered atoms. Specular x-ray diffraction (XRD) scans around typical (001) and (002) Bragg peaks for B2 ordered FeRh alloys show Pendellösung [21] fringes for films with $t_{\mathrm{FeRh}} \geq 5.2$ nm, which indicates nanothin FeRh alloys are very smooth and well-ordered densified single-crystal layers. The analysis of Pendellösung fringes reveals an offset thickness in the nanothin films, *i.e.* an Fe-enriched layer of ∼1.0-1.5 nm, as confirmed by the chemical mapping. Its origin resides in the segregation of Rh at the MgO/FeRh interface at elevated temperatures. Furthermore, chemical order increases with the FeRh thickness, t_{FeRh}, and the chemical order parameter, S, varies monotonically from 0.75 up to 0.9. The nanothin film's roughness varies from 0.6 down to about 0.1 nm as t_{FeRh} increases, and scales linearly with the integral breadth of the rocking curve, proving its microstructured origin. We show that the FOMPT is qualitatively similar to that of the bulk alloy, except for the nanothin film with t_{FeRh}=3.7 nm.

II. EXPERIMENTAL METHODS

Ultrathin FeRh films with thicknesses ranging from 3.7 nm up to 14.1 nm were deposited using a DC magnetron sputtering high vacuum (HV) chamber (typical base pressure $\sim 1 \times 10^{-6}$ Pa) onto (001)-oriented epi-polished MgO substrates 0.5-mm-thick, with a typical (001) deviation angle of 0.3° and surface roughness ≤ 0.5 nm. The deposition procedure is in essence similar to that previously reported [22]. Briefly, after degreasing and cleaning the MgO substrates in ultrasonic baths using acetone and isopropanol baths for 30 mins each at 308 K, these were baked and degassed at a temperature of 973 K for 1.5 hours in the HV chamber; after that, the substrate temperature was reduced to 873 K prior to deposition and maintained during the FeRh growth; immediately after finishing the FeRh alloy deposition, the as-grown nanothin films were annealed in HV at 1023 K for 2 h. At the deposition temperature, the sputtering chamber base pressure prior to deposition was $\sim 9 \times 10^{-6}$ Pa. The films were grown using a sputter gas (Ar) pressure of ∼ 0.1 Pa, with an Ar flow rate of ∼ 30 sccm. The dc voltage and current supplied by the magnetron power

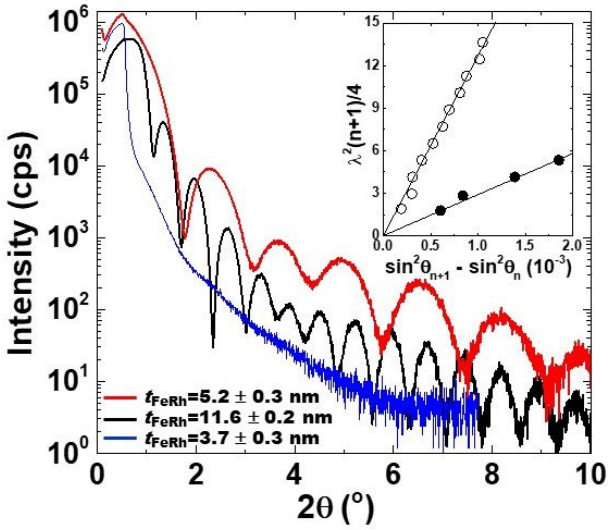

FIG. 1. X-ray reflectometry (XRR) scans for nanothin FeRh alloy films with FeRh thickness t_{FeRh} = 5.2 nm and 11.6 nm. t_{FeRh} was determined from the Kiessig fringe spacings [29]. The blue line corresponds to the XRR scan for the nanothin film with t_{FeRh} = 3.7 nm. Because of the absence of Kiessig fringes, its thickness was subsequently determined by using scanning transmission electron microscopy. The inset shows a linear fit of the Kiessig fringe spacing analysis for the films with t_{FeRh} = 5.2 nm (full dots) and 11.6 nm (empty dots).

source are about 365 V and 70 mA, respectively, resulting in a typical deposition rate of 0.25 nm s^{-1}. The FeRh target used was 2 inch in diameter and 3 mm thick and had a composition of $Fe_{47}Rh_{53}$ in at.% with a purity of 99.99%. In sputter-grown FeRh films, the composition in the deposited film measurably differs from that in the FeRh target used, so that the composition shift depends on the sputter gas pressure [23]. By extrapolating that measured sputter gas pressure dependence, we estimate from out known target composition that, in our case, the nanothin FeRh alloy film's composition is close to $Fe_{52}Rh_{48}$.

We opted not to use any capping layer to protect the nanothin FeRh films, in order to avoid it exerting influence upon the magnetic properties [24]. In fact, this common practice is unnecessary, provided the FeRh films are dense and compact enough. The formation of any significant native oxide layer at the FeRh surface is self terminating since, if it were to form, then it would leave Rh rich layers which are inert to oxidation. This way, the top outermost Rh layers in the FeRh alloy film act as an excellent corrosion resistance layer [27] for the underneath FeRh layers and native oxides are limited to only nanometer thickness

[24].

X-ray reflectometry (XRR) and diffractometry (XRD) θ-2θ scans, as well as ω-2θ rocking curves were collected in a four-circle diffractometer using a Cu Kα source. This has a V-Göbel mirror as a beam conditioner and a 2-bounce germanium monochromator, which results in an extremely parallel (divergence 0.007°) and monochromatic beam for high resolution measurements.

Atomic force micrographs were collected in non-contact mode, at a resolution of 512×512 pixels with a scanning frequency of 1 Hz. Commercial cantilever probes with a resonance frequency around 320 kHz were used. Raw data processing (background subtraction, flattenening and filtering) and the subsequent analysis of the AFM micrographs was performed using GWYDDION software[28].

A cross-sectional transmission electron microscopy (TEM) specimen of the 3.7 nm-thick FeRh film was prepared from the bulk substrate, transferred onto a copper Omniprobe grid and ion-milled using an FEI Nova focused ion-beam (FIB) instrument. Standard Ga^+ FIB operating procedures were followed (including final polishing steps, adding a Pt protective e-beam deposited layer and to reduce thickness of damaged sections) to produce an electron transparent FeRh/MgO lamella. TEM imaging and spectroscopy described in this paper were carried out on a JEOL Atomic Resolution Microscope (JEM-ARM200F) TEM, operating at 200 kV. Conventional and high-resolution high angle annular dark field (HAADF) scanning TEM (STEM) were performed on the cross-sectional TEM lamella and electron energy loss spectroscopy (EELS) provided chemical analysis.

Magnetization versus temperature scans were collected at a fixed applied magnetic field using a SQUID-VSM magnetometer. The temperature was swept at a typical rate of 2 K/min.

III. RESULTS AND ANALYSIS

We attempted to use the XRR technique [29] to experimentally determine the thickness of nanothin FeRh alloy films presented in this study, instead of relying on their estimated nominal thickness. Data are shown in Fig. 1. However, Kiessig fringes were absent from the XRR scan collected from the thinnest (t_{FeRh}=3.7 nm). In that case, the STEM technique was employed to determine its thickness by direct imaging of the cross-section of the film,

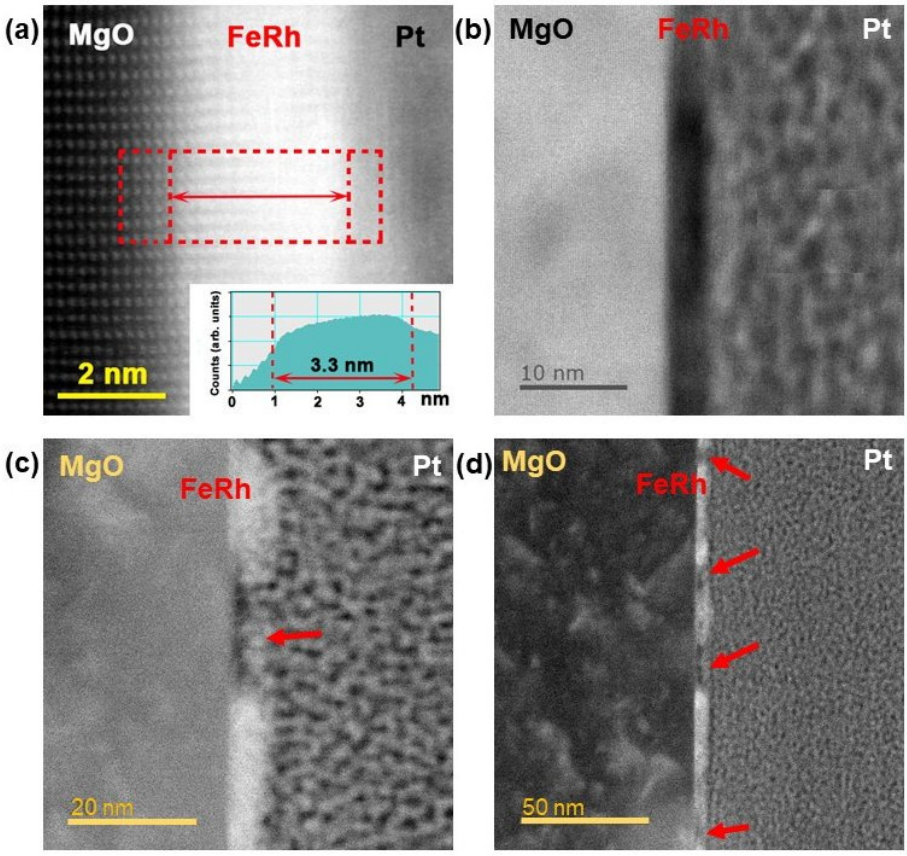

FIG. 2. HAADF-STEM images of a cross-sectional TEM lamella showing the FeRh thin film (middle of each image) grown on the MgO substrate (left), with an average thickness of 3.7 nm, and protective Pt layer (right). (a) High resolution HAADF-STEM image showing the localized structure of the FeRh and its epitaxial interface with the MgO substrate, as well as an average thickness profile (inset). HAADF-STEM images showing (b) a zone with uniform thickness and (c-d) others with non-uniform FeRh thin film, the discontinuous growth features denoted with red arrows.

shown in Fig. 2. Thus, the thicknesses of the remaining FeRh alloy films were determined from the Kiessig fringe spacings, so that the positions, *i.e.* θ values, for the maxima of the interference fringes are linked to the t_{FeRh} by the modified Bragg equation, which reads as [29]: $\sin^2\theta_{\mathrm{n}} = \theta_{\mathrm{c}}^2 + (n+1/2)^2\lambda^2/4t_{\mathrm{FeRh}}^2$ where θ_{n} is the position of the maximum of the n^{th} interference fringe, θ_{c} is the critical angle for total reflection, n is an integer, and $\lambda = 1.54184$ Å is the x-ray wavelength. This way, plotting $\lambda^2(n+1)/4$ *vs* $\sin^2\theta_{\mathrm{n+1}} - \sin^2\theta_{\mathrm{n}}$ removes the dependence on θ_{c}, so that the slope of the linear fit provides t_{FeRh} (see Fig. 1), which was determined to be $t_{\mathrm{FeRh}} = 4.1$, 5.2, 8.1, 9.2, 11.6 and 14.1 nm. As shown in

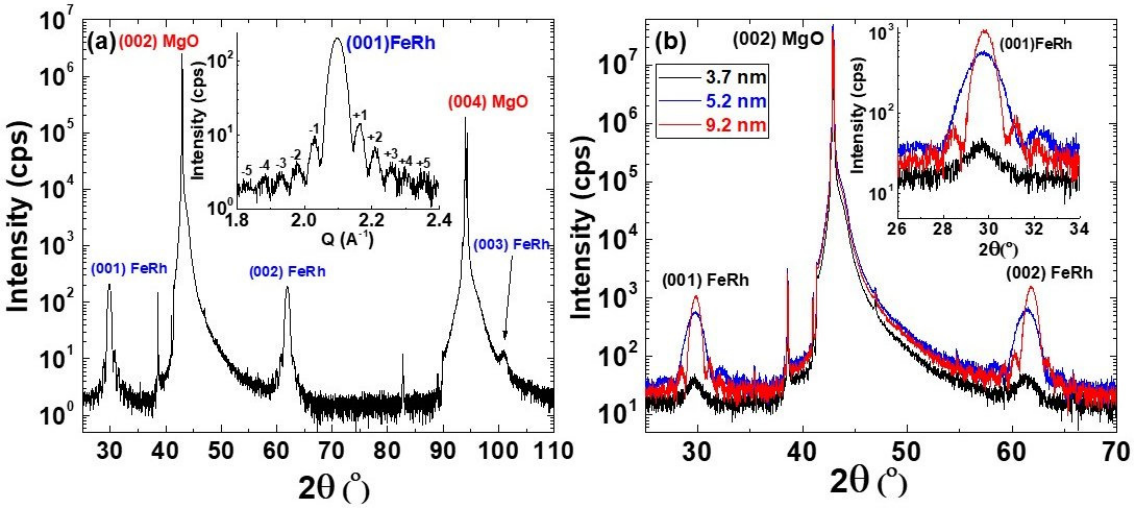

FIG. 3. Specular x-ray diffraction (XRD) θ-2θ scans for (001)-oriented FeRh alloy films grown onto (001)-oriented MgO single crystal substrates for FeRh thickness (a) $t_{\mathrm{FeRh}} = 14.1$ nm, where the inset shows a close-up of the XRD scan around the (001) Bragg peak as a function of the scattering wave-vector $\boldsymbol{Q}$. Well-developed Pendellösung fringes up to fifth-order are labeled. (b) As above for $t_{\mathrm{FeRh}} = 3.7$, 5.2, and 9.1 nm, where the inset displays a close-up of the XRD scan around the (001) Bragg peak.

Figure 1, XRR profiles collected for FeRh nanothin films with $t_{\mathrm{FeRh}} \geq 5$ nm clearly show well-defined Kiessig fringes up to high 2θ values, despite the reflectivity intensity decays as θ^4. This observation is an early indication of a smooth top surface, since Kiessig fringe intensity tends to decay quite rapidly with increasing surface roughness [30]. We note that the Kiessig fringe amplitude presents a subtle convoluted modulation (see Figure 1), which suggests the FeRh films possess a chemical modulation.

Figure 2(a) shows a high resolution HAADF-STEM image of the epitaxy across the MgO/FeRh interface for the nanothin film with $t_{\mathrm{FeRh}} = 3.7$ nm; the inset displays an average thickness profile in a slightly thinner zone of the film [see Fig. 2(a)]. As the field of view (FOV) of the HAADF-STEM increases, the FeRh film, which looked smooth and continuous at a FOV of 40 nm [see Fig. 2(b)], start to show regions of non-growth and inhomogenous thickness [see Figs. 2(c) and 2(d)]. The lateral dimensions of these regions range from 5 nm to a few tens of nm.

All sputter-grown nanothin FeRh alloy films are excellent-quality B2-ordered single crystals, as can be inferred from the specular XRD scans displayed in Fig. 3, wherein

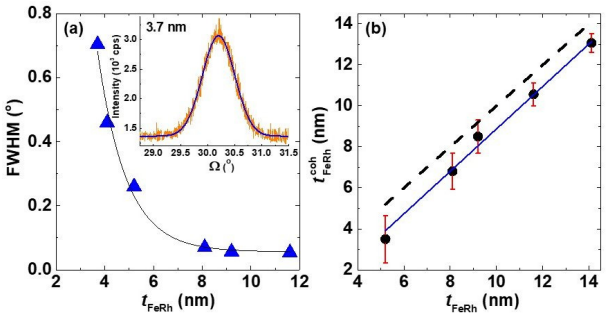

FIG. 4. Rocking curve analysis. (a) Dependence of the full-width-half-maximum (FWHM), measured over the rocking curve scan collected on the (002) FeRh Bragg peak, with the FeRh thickness, t_{FeRh}. The line is a guide to the eye. The inset shows the rocking curve scan collected on the film with t_{FeRh} = 3.7 nm. The line corresponds to a Gaussian fit with FWHM= 0.7° (b) Coherent FeRh thickness, $t^{\mathrm{coh}}_{\mathrm{FeRh}}$, determined as $2\pi/\Delta Q$ [31, 32] , where ΔQ is the spacing between adjacent Pendellösung fringes, as a function of the experimental t_{FeRh} values. The dashed line corresponds to a plot where $t^{\mathrm{coh}}_{\mathrm{FeRh}}$=$t_{\mathrm{FeRh}}$ and the continuous one is a guide to the eye.

(00l) for l=1, 2, and 3, Bragg diffraction peaks are observed. The expected epitaxial relationship between the MgO substrate and FeRh overlayer along the growth direction, MgO(002)‖FeRh(002), is observed, as can be inferred from Fig. 3. Furthermore, the (001) and (002) Bragg diffraction peaks for the B2-ordered FeRh alloys appear at values of the scattering angle, 2θ, around about 29.5° and 61.5°, respectively. Specular XRD scans collected in films with $t_{\mathrm{FeRh}}\geq$5.2 nm showed clear Pendellösung interference fringes[21] (*i.e.* Laue oscillations) around (001) and (002) Bragg peaks, but these are missing for $t_{\mathrm{FeRh}} < 5.2$ nm (see insets in Fig. 3). Thus, Pendellösung fringes firstly emerge as weak satellite peaks around (001) and (002) Bragg peaks in the 5.2 nm-thick FeRh film, wherein up to 2nd-order satellites are visible, and these grow in number and intensity as t_{FeRh} increases. Figure 3(a) shows well-developed Pendellösung fringes around (001) Bragg peak up to fifth-order in the film of 14.1 nm thickness. Pendellösung fringes are absent in films with t_{FeRh} = 3.7 and 4.1 nm, which may result from a crystallinity degradation of the FeRh films as these get thinner, resulting from a rougher top-surface, a smaller grain size and a larger mosaicity. However, we highlight that the appearance of Pendellösung fringes in our nanothin films is a feature not found at all in prior studies reporting on nanothin FeRh films [15–19]. Additionally, these XRD scans show no trace of the Bragg peak associated with the fcc γ-FeRh

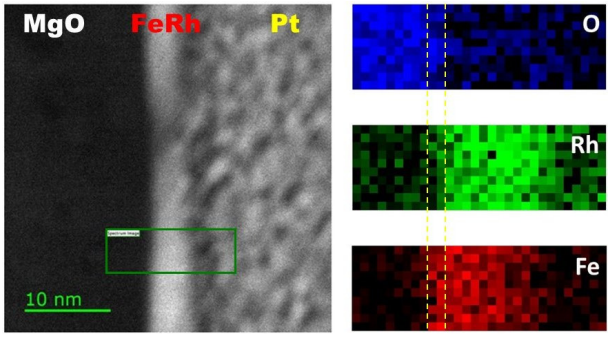

FIG. 5. HAADF-STEM analysis. (Left-panel) HAADF-STEM image showing the MgO substrate (lefthand portion of the image), FeRh layer (middle) and protection Pt layer (right) for the film with $t_{\mathrm{FeRh}} = 3.7$ nm. (Right-panel) Chemical composition mapping for oxygen, rhodium, and iron, obtained using EELS (pixel lateral size is 5 Å) over the area enclosed by the green box (longside length is ~ 15 nm) in the left-panel. The 1 nm-thick Fe-enriched layer is denoted by yellow dashed lines.

phase, which should appear at around about $2\theta \sim 47°$ (assuming that $a_{\text{fcc-FeRh}} \sim 0.37$ nm).

Rocking curve ω-2θ scans have been collected over the (002) FeRh Bragg peaks to check the film's grain size and mosaicity along growth direction, *i.e.* the measure of the spread or tilt of (001) crystal plane orientations, which gives an accurate indication of the degree of crystallinity of the nanothin films. As displayed in Fig. 4(a), the variation of the full-width-half-maximum (FWHM) of the rocking curve with t_{FeRh} shows two distinct regimes. It is found that the integral-breadth or FWHM is around 0.06° for $t_{\mathrm{FeRh}} \geq 8.1$ nm, but this increases rapidly for $t_{\mathrm{FeRh}} \leq 5.2$ nm yielding FWHM= 0.7° for $t_{\mathrm{FeRh}} = 3.7$ nm. Fig. 4(b) shows the coherent FeRh thickness, $t^{\mathrm{coh}}_{\mathrm{FeRh}}$, determined as [31, 32], $t^{\mathrm{coh}}_{\mathrm{FeRh}} = 2\pi/\Delta Q$, where ΔQ is the spacing between consecutive Pendellösung fringes emerging around the (001) Bragg peak in reciprocal space. We notice that unlike the (002) Bragg peak, which has its origin in the bcc lattice, the (001) one is exclusively linked to the B2 ordering. Thus, we observed that in all cases $t^{\mathrm{coh}}_{\mathrm{FeRh}} < t_{\mathrm{FeRh}}$; moreover, the difference between the FeRh thickness and the coherent one, $\Delta t = t_{\mathrm{FeRh}} - t^{\mathrm{coh}}_{\mathrm{FeRh}}$ ranges from 1.6 nm ($t_{\mathrm{FeRh}} = 5.2$ nm) down to 1 nm ($t_{\mathrm{FeRh}} = 14.1$ nm). The emergence of such "offset" thickness, Δt, which to first-order approximation could be considered as thickness-independent (notice the uncertainty in the data in Fig. 4(b)), it is tentatively ascribed to a MgO/FeRh interface effect, resulting from the segregation of Fe and Rh metal species at the interface, as confirmed by the chemical

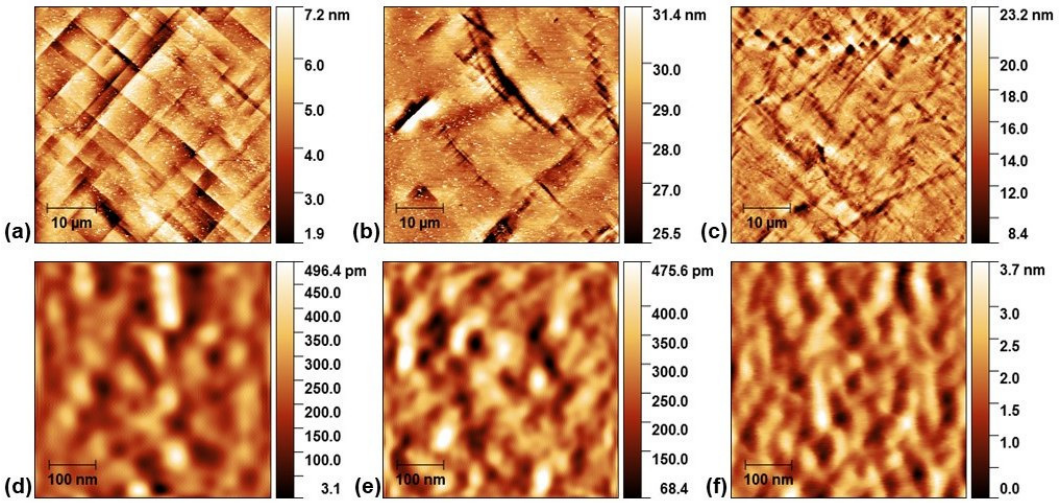

FIG. 6. Atomic force micrographs taken on nanothin FeRh alloy films with FeRh thickness, $t_{\mathrm{FeRh}} =$ 14.1 nm, (a) and (d), $t_{\mathrm{FeRh}} = 9.2$ nm, (b) and (e), and $t_{\mathrm{FeRh}} = 3.7$ nm, (c) and (f). AFM scan size is 50×50 µm^2 (top row) and 0.5×0.5 µm^2 (bottom row); micrographs edges are aligned along the [110]MgO‖[100]FeRh and [$\bar{1}$10]MgO‖[010]FeRh directions. Height scales have been set to optimize image contrast.

mapping across the MgO/FeRh interface (see Fig. 5). Thus, within the resolution provided by EELS, we estimate that the thickness of the FeRh layer near to the MgO/FeRh interface, which seems to be richer in Fe, is $\sim$ 1.0-1.5 nm, which is consistent with Δt. Segregation-driven processes at the interfaces of bimetallic alloy systems, resulting from the dissimilar stability of metal species in oxidizing environments, is a familiar mechanism in catalysis [33]. Building on that, we attribute the segregation of Fe and Rh at the MgO/FeRh interface during film growth and annealing to the instability of Rh-O bonds [25, 34] at $T > 600$°C. Therefore, we can conclude that there exists in principle a good correlation between the increase of the integral-breadth of the rocking curve in the thinnest films and the absence of Pendellösung fringes. We note that little noticeable evidence for any native oxide layer, suggesting that it must be extremely thin if present at all.

In sharp contrast to prior studies [15–19], our sputter-grown nanothin FeRh films show a smooth surface morphology, as shown in Fig. 6. There we show atomic force micrographs that show that the FeRh layer wets completely the MgO surface with the exception of the very thinnest films, *i.e.* for those with $t_{\mathrm{FeRh}} < 5$ nm. These very thin films present a rougher morphology than the thicker ones and show small regions of incomplete coverage or pits,

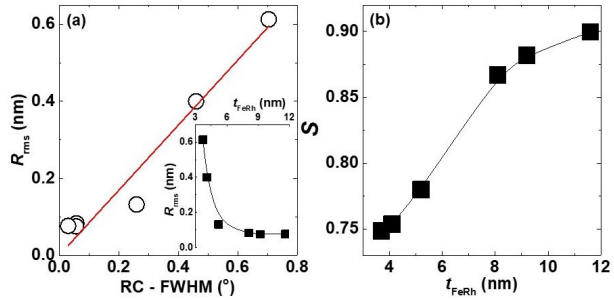

FIG. 7. Structural analysis. (a) Average root-mean-square roughness, R_{rms}, versus full-width-half-maximum (FWHM) of the rocking curve. The line corresponds to a linear fit, where the intercept is zero and the slope is to 0.845 ± 0.056 nm/deg. Standard deviation values for the R_{rms} are smaller than or similar to the dots size. The inset shows the variation of R_{rms} with t_{FeRh}. (b) Thickness dependence of the nanothin FeRh alloy films order parameter, S, determined according to Ref. 35.

with lateral dimensions ranging from 5 to $\sim$ 30 nm, as shown for the 3.7 nm-thick film. Strikingly, this observation suggests that the sputter-grown nanothin FeRh layers deposited at low Ar pressure tend to grow in an induced Frank-van der Merwe growth mode for thicknesses above 5 nm, in marked contrast to the Volmer-Weber growth mode reported previously [15–19]. The atomic force microscopy (AFM) images taken for a scan size of 50×50 μm^2 reveal that the FeRh overlayers develop a terrace-like pattern, which could be mistakenly assigned to the expected presence of atomic-steps at the bottom epi-polished (001) MgO surface. However, as the experiment shows, these terrace-like features are $t_{\rm FeRh}$ dependent [see Figs. 6(a)-6(c)], starting to emerge for $t_{\rm FeRh} > 5$ nm and vanishing for the thinnest films. Therefore, we conclude from this observation that terrace-like features are not carried through from the substrate, but emerge from the crystallographic structure of the FeRh films as the surface smooths out. Bear in mind that AFM image edges are aligned ($\pm 5^\circ$ misalignment) along the [110]MgO$\|$[100]FeRh and [$\bar{1}$10]MgO$\|$[010]FeRh directions in the MgO substrate and FeRh film (notice the 45° rotation between the MgO and FeRh cubic lattices [19]). AFM micrographs with scan size 0.5×0.5 μm^2 exhibit an astonishing similarity, except for the depth of the regions of inhomogeneous thickness, which become pits through the whole thickness for the thinnest film [see Figs. 6(d)-6(f)]. Therefore, the surface morphology features revealed by the AFM micrographs are consistent with the STEM images taken on the thinnest FeRh film.

The average root-mean-square roughness, $R_{\rm rms}$, was determined using the GWYDDION

software [28] over several 0.5×0.5 μm^2 AFM micrographs taken at different places on each film's surface. This scan size ensures the $R_{\rm rms}$ is determined within an FeRh terrace. As shown in Fig. 7(a), there is a clear correlation between the integral-breadth of the rocking curve, *ie* FWHM, and $R_{\rm rms}$ in the nanothin FeRh films, which suggests the $R_{\rm rms}$ has its origin in the film microstructure, this is grain size and mosaicity. The chemical order parameter S is a measure of the ordering quality possessed by the nanothin FeRh alloy films, and is defined as the fraction of Fe/Rh lattice sites in the B2 crystallographic structure that obey the ordering condition, $S = r_{\rm Fe} + r_{\rm Rh} - 1$ where $r_{\rm Fe(Rh)}$ is the fraction of Fe(Rh) lattice sites occupied by Fe(Rh) atoms. From the specular XRD scans, S can be determined as, $S = \left(\left[(I_{(001)}/I_{(002)} \right] / \left[I^*_{(001)}/I_{(002)^*} \right] \right)^{1/2}$, where $I_{(002)}$ and $I_{(001)}$ are the integrated intensities of the fundamental and superlattice Bragg peaks, respectively, and the $I^*_{(001)}$ and $I^*_{(002)}$ refer to the theoretical ones, calculated for each sample [35]. We note that I^* is a function of $t_{\rm FeRh}$, the integral-breadth of the Bragg peaks, and the divergence and goniometer radius of the x-ray diffractometer. If S is calculated otherwise [22], S will attain values well above unity for all the nanothin films in this study, which lacks meaning, as $S \leq 1$ by definition. As displayed in Fig. 7(b), S decreases as films are thinner, ranging from nearly 0.9 for the thickest films down to 0.75 for the thinnest, which indicates that the chemical order degrades as films get thinner, although these are chemically well ordered B2 FeRh alloys, despite their finite-size.

Fig. 8(a) shows in-plane magnetization as a function of temperature (M-T) curves for nanothin FeRh alloy films with $t_{\rm FeRh}$ = 3.7, 5.2, 8.1 and 9.2 nm, wherein the sharp rise in M associated the FOMPT in FeRh[6] is clearly observed. The criterion for determining the FOMPT temperature, $T_{\rm MPT}$, from the M-T curves consists of obtaining the point over the M-T locus that yields the maximum slope. It turns out that $T_{\rm MPT}$ is shifted towards lower temperatures, consistent with prior studies[16], and the FOMPT width, ΔT, becomes broader as $t_{\rm FeRh}$ decreases. Although further research is needed, this latter aspect may reflect in the impact that finite-size effects have upon the FOMPT [36]. We find that $T_{\rm MPT}$ = 359, 302, 281 and 298 K and ΔT = 30, 68, 136 and 170 K for $t_{\rm FeRh}$ = 9.2, 8.1, 5.2 and 3.7 nm, respectively, measured all over the M-T curve on cooling. The residual M in the AF phase, which is linked to the presence of B2 disordered FeRh phase clusters and, therefore, intimately related to S [37], appears to increase as the films become thinner [see Fig. 8]. A plausible reason for that could be that there is a small region of crystalline

degradation of the B2 ordered structure near the interface that forms a larger and larger proportion of the film as it becomes thinner, which is also reflected in the diminishing value of S as film's thickness decreases (see Fig. 7(b)). Besides, the M values for films with $t_{\mathrm{FeRh}} \geq 5.2$ nm attain in excess of 900 emu cm^{-3} in the FM phase, smaller than that in bulk FeRh [6], $\sim$ 1200 emu cm^{-3}, but notably larger than those values obtained in similar FeRh films [16–19].

Building on the suppression of the AF-FM transition in FeRh nanoparticles [38], we foresee that the likely presence of strain gradients in our nanothin films, anticipated by the thickness-dependence of the (001) and (002) Bragg peak breadths as seen in Fig. 3(b), may surely contribute to increase the observed residual FM moment in the AF phase. Following with this analogy, the existence of a strain-induced lattice parameter relaxation mainly along the growth direction, would affect the highly sensitive interatomic distance dependent AF-FM exchange coupling balance, resulting in setting a non-uniform thickness-dependent AF-FM phase coexistence. Studying this matter in more depth is well beyond the scope of the present study; we hope however that our work might inspire further studies to shed light on this issue using advanced characterization tools, *i.e.* Bragg coherent diffraction imaging or differential nano-X-ray absorption spectroscopy.

Likewise, it is remarkable that the large diminishment of the in-plane M shown by the 3.7 nm-thick FeRh film, in comparison to those values attained in thicker films (see Figure 8), was also observed in similar nanothin films, displaying a rough morphology and having a smaller order parameter [19]. In first instance, we should consider that nanothin FeRh films deposited onto single-crystal MgO substrates are prone to developing a strong perpendicular magnetic anisotropy originated at the FeRh/MgO interface, caused by the formation of an Fe-enriched layer close to the MgO substrate [39]. This way, we envisage competing surface and volume magnetic anisotropy terms would induce a tendency for the magnetisation to tilt out-of-plane as the film thickness becomes small. Whilst for films with $t_{\mathrm{FeRh}} \geq 5.2$ nm, the easy direction for M clearly lies in-plane, for the film with $t_{\mathrm{FeRh}} = 3.7$ nm, the remanent M for $\mathbf{H}\|[001]$, i.e. $M_{\mathrm{r}}^{[001]}$, is twice as much as $M_{\mathrm{r}}^{[110]}$. In this thinnest film, M attains dissimilar saturation values for H applied in- and out-of-plane (see Fig. 8(b)), resulting in a nearly 40% larger M for $\mathbf{H}\|[001]$, which would partially contribute to the substantial reduction of the M values in Fig. 8(a), when compared to those in the thicker films. On the other hand, the $M(H)$ loop for $\mathbf{H}\|[110]$ is more upright and saturates at a lower field than that for $\mathbf{H}\|[001]$,

where there is a long gradual approach to saturation. This mixed evidence for where the easy direction lies suggests that the anisotropy is also mixed and lateral inhomogeneities are likely to exist in this very thin film. This may in part be do to with variations in the degree of oxidation: the thinness of any oxide layer, as discussed above, means that is not likely to be continuous and uniformly well-developed everywhere across the whole film surface.

Another crucial aspect to consider in FeRh nanosystems is the influence that non-uniform strains and low-dimensionality effects may have, both on the anisotropy and also upon reducing M. Thus for instance, in unstrained 3.3 nm diameter FeRh nanoparticles, a 10% reduction of the magnetic moment is observed [38]. (Notice that a broader spread of the lattice parameter is intrinsically expected for the highly-strained 3.7-nm-thick film.) We anticipate the origin of the anisotropy of M resides in a strain-induced spin-orbit-mediated anisotropic $3d$-$4d$ hybridized [42] orbital filling [43] in tetragonally distorted FeRh films. We notice that the anisotropy of the magnetic moment is not an atypical phenomenon, especially when dealing with strained nanostructures [44] or materials that hold a strong spin-orbit coupling [45]. Ultrathin FeRh films provide a fertile ground for investigating emergent strain-induced anisotropies, given that they combine a relatively large spin-orbit coupling [42] with the feasibility of developing substantial epitaxial strains [19].

IV. DISCUSSION

The microstructure of sputter-grown thin films can be tailored, to a great extent, by adequately choosing sputtering deposition parameters, mainly sputter-gas (Ar) pressure, p_{Ar}, and substrate temperature [50, 51], T_{subs}. From earlier studies [15–19], it is known that epitaxial nanothin FeRh films deposited onto single-crystal MgO substrate tend to grow in the Volmer-Weber growth mode [52]. These experimental results can be qualitatively understood, neglecting the effect associated to the misfit strain ($< 0.5\%$) between FeRh and MgO, in terms of the surface free energy [53], γ, associated to the system formed by the (001) MgO substrate surface [54], $\gamma_{\mathrm{subs}}^{\mathrm{MgO}} = 1.1$ Jm^{-2}, (001)Fe [55] and (001)Rh [55] overlayers/film, $\gamma_{\mathrm{f}}^{\mathrm{Fe}} = 2.94$ Jm^{-2} and $\gamma_{\mathrm{f}}^{\mathrm{Rh}} = 2.83$ Jm^{-2} respectively, and substrate-overlayer interface, $\gamma_{int}^{MgO-FeRh}$. In this case, the Volmer-Weber growth mode occurs because $\gamma_{\mathrm{subs}}^{\mathrm{MgO}} < \gamma_{\mathrm{f}}^{\mathrm{Fe}}$ (or $\gamma_{\mathrm{f}}^{\mathrm{Rh}}$)+$\gamma_{\mathrm{int}}^{\mathrm{MgO\text{-}FeRh}}$, where the FeRh overlayer tends not to wet the MgO surface, randomly nucleating dome-like atom clusters. As the effective thickness increases, the initially FeRh

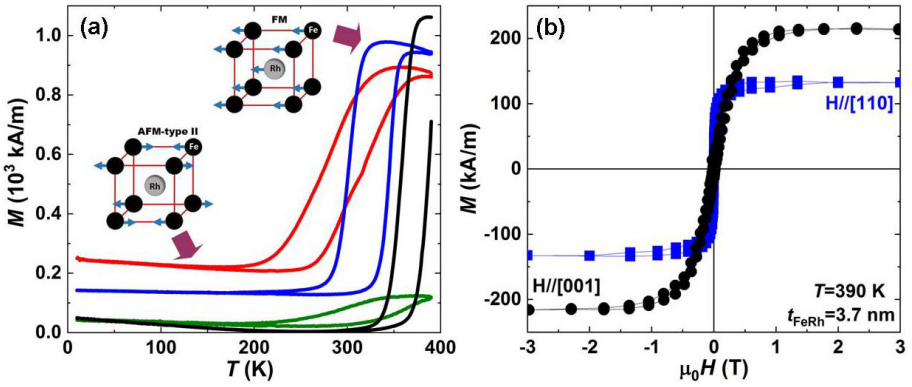

FIG. 8. Magnetic properties. (a) Magnetization as a function of temperature for FeRh alloy films with thickness, $t_{\mathrm{FeRh}} = 9.2$ (black), 8.1 (blue), 5.2 (red) and 3.7 nm (green) for an applied magnetic field, $\mu_0 H_{\mathrm{app}} = 0.1$ T so that $\mathbf{H}\|[110]$. (b) M-H loops for $\mathbf{H}\|[110]$ (blue squares) and $\mathbf{H}\|[001]$ (black dots) for the thinnest film in the FM phase.

clusters increase in size, developing into islands, which grow predominately faster in height than in lateral size, and eventually forming an almost continuous layer only for thick FeRh films, where FeRh islands coalesce.

A plausible way to circumvent the unwanted Volmer-Weber growth mode observed in FeRh overlayers consists of sputter-growing FeRh at low p_{Ar}. During sputtering deposition, the sputtered atoms are ejected with average energies of the order of ~ 10 eV [56–59], which compare well with the sublimation energy for Fe/Rh metal species, $\sim$ 4-7 eV [60]. A substantial loss of kinetic energy by the ejected sputtered atoms is expected at elevated p_{Ar}, typically > 0.65 Pa in most cases, due to collisions (thermalization effect) with plasma particles and sputter-gas atoms while travelling from the cathode towards the substrate. However, such energy loss at low p_{Ar}, typically < 0.15 Pa in most cases, is in turn negligible, which entails major microstructural transformations for the condensed overlayer, since its surface is relentlessly bombarded by highly-energetic particles, including the ejected sputtered atoms, an effect known as *atom-peening* [20]. This unique aspect of sputtering deposition technology has been experimentally [61] and theoretically [62, 63] tested.

Besides T_{subs} and p_{Ar}, morphology and microstructure of sputter-grown FeRh films finely depend on other sputtering deposition parameters [64], such as the deposition power P, in addition to substrate-to-target distance, L, which together with P determines the deposition rate, $\sim P/L$, and the magnetron design, which determines the minimum p_{Ar} needed to

sustain the plasma. To illustrate that point, in our sputtering facility Ar gas is injected directly over the face of the target, which enables us to sustain the plasma even for $p_{\mathrm{Ar}} = 0.06$ Pa at $P = 20$ W. It is enlightening at this point to introduce the mean free path of the FeRh sputtered atoms, $\bar{l}_{\mathrm{FeRh}}$, *i.e.* the mean distance that the sputtered atoms travel in the plasma and Ar gas before suffering a collision and start losing kinetic energy. $\bar{l}_{\mathrm{FeRh}}$ can be related to p_{Ar} as [65, 66]: $\bar{l}_{\mathrm{FeRh}} = \frac{k_B T}{\sqrt{2}\pi p_{\mathrm{Ar}} d_{\mathrm{m}}^2}$, where k_{B} is the Boltzmann constant, T is the sputtering gas temperature and d_{m} is the molecular diameter of Ar gas (~ 0.4 nm). Thus, for $p_{\mathrm{Ar}} = 0.1$ Pa and at room temperature, $\bar{l}_{\mathrm{FeRh}} \simeq 6.44$ cm. Moreover, the dimensionless Knudsen number, K_{n}, is defined as [65], $K_{\mathrm{n}} = \bar{l}_{\mathrm{FeRh}}/L$, for sputtering deposition, and characterizes the regime at which the sputtering deposition takes place. Thus, for $K_{\mathrm{n}} \geq 1$, the sputtering deposition process occurs in the high vacuum regime, *i.e.* the sputtered Fe and Rh atoms bombard the condensed layer on the substrate as highly energetic atoms. Conversely, for $K_{\mathrm{n}} < 0.01$ sputtering deposition takes place in the fluid flow regime, this is the sputtered atoms are mostly thermalized. For intermediate K_{n} values, which is the most common situation, the sputtering deposition takes place in the transition regime. Thus, K_{n} is largely a sputtering deposition conditions independent value, which could be envisioned as a quantitative manner of comparing sputtering deposition processes. In our sputtering facility and for $p_{\mathrm{Ar}} = 0.1$ Pa, K_{n} is 0.915, which clearly denotes that the atom-peening effect is the dominant factor that determines the morphology and microstructure of the sputter-grown layer.

During the deposition at low p_{Ar} ($\sim$0.1 Pa) of the FeRh nanothin films, they are constantly bombarded by energetic sputtered Fe and Rh atoms, which concomitantly incorporate to the condensed FeRh layer. This *atom-peening* effect [20] decisively affects the deposited FeRh layer microstructure [20, 61, 67], *e.g.* it induces layer densification, significantly improves the crystallinity, as well as introduces compressive strain in the deposited overlayer. This is because the kinetic energy which sputtered Fe and Rh atoms impact with on the FeRh overlayer is high enough to displace previously deposited Fe and Rh atoms from their equilibrium positions at the surface. In a way, the atom-peening effect forces a re-balancing of the thermodynamic equilibrium between adsorbate-surface and adsorbate-adsorbate interactions, originally leading to the Volmer-Weber growth mode. For the sake of clarity, we notice that at the FeRh deposition temperature used here, *i.e.* $T_{\mathrm{dep}} = 873$ K, the reduced temperature $T_{\mathrm{dep}}/T_{\mathrm{melt}} \simeq 0.46$, where $T_{\mathrm{melt}} \sim 1900$ K [68] is the melting temperature for

FeRh alloy, which indicates that during the FeRh deposition thermodynamic equilibrium is reached, where atom diffusion at the surface is the dominant process [50, 51]. Therefore, by depositing at low sputter-gas pressures, the atom-peening effect causes the initially nucleated FeRh islands to undergo a smoothing and planarization process. Thus, the FeRh islands are forced to grow mainly in the lateral dimensions, rather than in height, as a result of the bombardment pressure exerted by the highly energetic sputtered atoms, so that the deposited FeRh layer covers most of the MgO surface by forcing FeRh islands to coalesce at very low nominal deposition thickness. Simultaneously, the FeRh layer is densified and its degree of single-crystal perfection increased [69]. Our nanothin FeRh films present a microstructure and surface morphology, revealed by XRD, AF micrographs and STEM images, that is fully compatible with the aftermath of the atom-peening effect. Moreover, the strikingly good crystallinity observed in the sputter-grown FeRh nanothin films described here, *i.e.* the appearance of Pendellösung fringes, a smooth surface, and the induced Frank-van der Merwe growth mode, which takes place for $t_{\mathrm{FeRh}} > 5$ nm, is therefore a direct consequence of the above-mentioned atom-peening effect.

According to kinetic roughening theory [70, 71], the root-mean-square surface roughness, R_{rms}, scales with the thin films thickness, T, as a power-law [72], $R_{\mathrm{rms}} \propto t^{\beta}$, where β takes different values, typically between 0 and 1, depending on the growth mode [71, 73]. This implies that R_{rms} increases as thin films grows thicker, since $\beta > 0$. However, we experimentally observe an opposite behavior in our nanothin FeRh films, so that R_{rms} decreases as t increases, as displayed in Fig. 7(a). Besides, we find that the R_{rms} scales linearly with the rocking curve FWHM (see Fig. 7(a)), which indicates that the film surface roughness originates in its microstructure, *i.e.* grain size and mosaicity. Notice that the finite-size of the diffraction volume and tilt of crystal planes both inseparably contribute to the broadening of the rocking curves [31]. We tentatively assign this unusual trend to the smoothing, flattening and densification processes that occur in the nanothin FeRh film as result of the atom-peening effect [69]. Film thickness is controlled by deposition time, and both are linearly related, so that the thicker the film the longer the FeRh overlayer is exposed to the atom-peening effect. We can therefore infer from the above that the island coalesce, overlayer densification and surface smoothing are thickness-dependent effects, since atom-peening process impacts primarily on the outermost FeRh layers. Thus, we interpret the data shown in Fig. 7(a) as a growth regime transition from a rougher almost continuous film

(Volmer-Weber type growth mode) at low nominal t_{FeRh} to a smoother densified continuous (peening-induced Frank-van der Merwe growth mode) for thicker films, with an inflection point for about $t_{\mathrm{FeRh}} = 5$ nm. Lastly, the thickness variation of the chemical order parameter displayed in Fig. 7(b) is most likely related to the formation of an Fe-enriched layer, caused by the Rh segregation at the MgO/FeRh interface, which may also affect the B2 ordering in the FeRh layers above.

V. CONCLUSIONS

In summary, we have shown that, in sharp contrast to prior studies [15–19], sputter-grown sub-15-nm-thick FeRh alloy films deposited at low sputter-gas pressure, typically ~ 0.1 Pa, onto (001)-oriented MgO substrates grow in a modified Volmer-Weber type growth mode, turning this into an atom-peening-induced [20] Frank-van der Merwe growth mode for thicknesses above 5 nm. This growing procedure considerably improves the film crystallinity, which decisively contributes to preserving the first-order magnetic phase transition in the nanothin films. Thus, the chemical order increases with the FeRh thickness, t_{FeRh}, and varies monotonically from 0.75 up to 0.9. Furthermore, specular XRD scans around Bragg peaks display Pendellösung interference fringes [21] for films with $t_{\mathrm{FeRh}} \geq 5.2$ nm, which reflects in smooth well-ordered densified single-crystal FeRh layers. Surface morphology in the nanothin FeRh alloy films is smooth and FeRh layers tend to form a continuous film, even at very low thicknesses, uniformly wetting the whole MgO surface for $t_{\mathrm{FeRh}} > 5$ nm. Additionally, the root-mean-square roughness varies from 0.6 nm down to about 0.1 nm as t_{FeRh} increases, and scales linearly with the integral-breadth of the rocking curve measured on the (002) FeRh Bragg scattering peak, proving that its origin resides in the film's microstructure. Iso-field magnetization measurements show that the first-order metamagnetic phase transition is qualitatively similar to that of the bulk alloy, i.e. is sharp and shows little thermal hysteresis, in all nanothin films, although for the 3.7 nm-thick film this becomes broader, less sharp and is accompanied by a significant diminishing in the saturation magnetization value. Lastly, we would like to highlight that the thin film growth approach laid down here is of wide applicability and can be reliably used to grow, by means of sputtering techniques, smooth continuous compact densified nanothin metal overlayers onto insulating substrates, which will eventually enable to undertake novel exciting spintronics studies.

ACKNOWLEDGMENTS

The authors acknowledge funding support from the European Commission through a Marie Skłodowska-Curie Intra-European Fellowship (MSCA-IF-2016, Contract No. 748691) and the Engineering and Physical Sciences Research Council in the UK (Grants No. EP/M018504/1 and EP/M019020/1).

[1] A. Zylbersztejn and N. F. Mott, Metal-insulator transition in vanadium dioxide, *Phys. Rev. B* **11**, 4383 (1975).

[2] Z. Huang, S. Chena, C. Lv, Y. Huang, and J. Lai, Infrared characteristics of VO_2 thin films for smart window and laser protection applications, *Appl. Phys. Lett.* **101**, 191905 (2012).

[3] M. Fallot, Propiétés magnétiques des alliages du fer avec l'iridium, *C. R. Hebd. Seances Acad. Sci.* **205**, 517 (1937).

[4] M. Fallot, Propiétés magnétiques des alliages du fer avec le ruthénium et l'osmium, *C. R. Hebd. Seances Acad. Sci.* **205**, 227 (1937).

[5] M. Fallot, Propiétés magnétiques des alliages du fer avec le rhodium, *C. R. Hebd. Seances Acad. Sci.* **205**, 558 (1937).

[6] J. S. Kouvel and C. C. Hartelius, Anomalous magnetic moments and transformations in the ordered alloy FeRh, *J. Appl. Phys.* **33**, 1343 (1962).

[7] G. Shirane, R. Nathans, and C. W. Chen, Magnetic moments and unpaired spin densities in the Fe-Rh alloys, *Phys. Rev.* **134**, A1547 (1964).

[8] M. R. Ibarra and P. A. Algarabel, Giant volume magnetostriction in the FeRh alloy, *Phys. Rev. B* **50**, 4196 (1994).

[9] P. A. Algarabel, M. R. Ibarra, C. Marquina, A. del Moral, J. Galibert, M. Iqbal, and S. Askenazy, Giant room-temperature magnetoresistance in the FeRh alloy, *Appl. Phys. Lett.* **66**, 3061 (1995).

[10] L. H. Lewis, C. H. Marrows, and S. Langridge, Coupled magnetic, structural, and electronic phase transitions in FeRh, *J. Phys. D.: Appl. Phys.* **49**, 323002 (2016).

[11] X. Marti, I. Fina, C. Frontera, J. Liu, P. Wadley, Q. He, R. J. Paull, J. D. Clarkson, J. Kudrnovský, I. Turek, *et al.,* Room-temperature antiferromagnetic memory resistor, *Nat.*

Mater. **13**, 367 (2014).

[12] Y. Lee, Z.Q. Liu, J.T. Heron, J.D. Clarkson, J. Hong, C. Ko , M.D. Biegalski, U. Aschauer, S.L. Hsu, M.E. Nowakowski, *et al.,* Large resistivity modulation in mixed-phase metallic systems, *Nat. Commun.* **6**, 5959 (2015).

[13] J-U. Thiele, S. Maat, and E. E. Fullerton, FeRh/FePt exchange spring films for thermally assisted magnetic recording media, *Appl. Phys. Lett.* **82**, 2859 (2003).

[14] R. E. Rottmayer, S. Batra, D. Buechel, W. A. Challener, J. Hohlfeld, Y. Kubota, L. Li, B. Lu, C. Mihalcea, K. Mountfield, *et al.,* Heat-assisted magnetic recording, *IEEE Trans. Magn.* **42**, 2417 (2006).

[15] M. Loving, F Jimenez-Villacorta, B. Kaeswurm, D. A. Arena, C. H. Marrows, and L. H. Lewis, Structural evidence for stabilized ferromagnetism in epitaxial FeRh nanoislands, *J. Phys. D: Appl. Phys.* **46**, 162002 (2013).

[16] G. C. Han, J. J. Qiu, Q. J. Yap, P. Luo, T. Kanbe, T. Shige, D. E. Laughlin, and J.-G. Zhu, Suppression of low-temperature ferromagnetic phase in ultrathin FeRh films, *J. Appl. Phys.* **113**, 123909 (2013).

[17] G. C. Han, J. J. Qiu, Q. J. Yap, P. Luo, D. E. Laughlin, J. G. Zhu, T. Kanbe, and T. Shige, Magnetic stability of ultrathin FeRh films, *J. Appl. Phys.* **113**, 17C107 (2013).

[18] Q. J. Yap, J. J. Qiu, P. Luo, J. F. Ying, G. C. Han, D. E. Laughlin, J.-G. Zhu, T. Kanbe, and T. Shige, Phase ordering and its effect on magnetic and structural properties of FeRh ultrathin films, *J. Appl. Phys.* **116**, 043902 (2014).

[19] C. W. Barton, T. A. Ostler, D. Huskisson, C. J. Kinane, S. J. Haigh, G. Hrkac, and T. Thomson, Substrate induce strain field in FeRh epilayers grown on single crystal MgO (001) substrates, *Sci. Rep.* **7**, 44397 (2017).

[20] H. Windischmann, An intrinsic stress scaling law for polycrystalline thin films prepared by ion beam sputtering, *J. Appl. Phys.* **62**, 1800 (1987).

[21] A. R. Lang and M. Zhen-Hong, Pendellösung interference in the Bragg reflexion of X-rays from a crystal surface, *Proc. R. Soc. London Ser. A* **368**, 313 (1979).

[22] C. Le Graët, M. A. de Vries, M. McLaren, R. M. D. Brydson, M. Loving, D. Heiman, L. H. Lewis, and C. H. Marrows, Sputter Growth and Characterization of Metamagnetic B2-ordered FeRh Epilayers, *J. Vis. Exp.* **80**, e50603 (2013).

[23] M. Jiang, X. Z. Chen, X. J. Zhou, Y. Y. Wang, F. Pan and, C. Song, Influence of film composition on the transition temperature of FeRh films, *J. Cryst. Growth* **438**, 19 (2016).

[24] C. Baldasseroni, G. K. Pálsson, C. Bordel, S. Valencia, A. A. Unal, F. Kronast, S. Nemsak, C. S. Fadley, J. A. Borchers, B. B. Maranville, *et al.*, Effect of capping material on interfacial ferromagnetism in FeRh thin films, *J. Appl. Phys.* **115**, 043919 (2014).

[25] S. D. Cramer and B. S. Covino, Jr., eds. *ASM Handbook (vol. 13B), Corrosion: Materials* (ASM International 2005, p. 393–396).

[26] J. Emsley, *Nature's Building Blocks* (Oxford University Press 2001, p. 363).

[27] A. M. Weisberg, Rhodium plating, *Metal Finishing* **97**, 296 (1999).

[28] D. Nečas and P. Klapetek, Gwyddion: An open-source software for SPM data analysis, *Cent. Eur. J. Phys.* **10**, 181-188 (2012).

[29] T. C. Huang, R. Gilles, and G. Will, Thin-film thickness and density determination from X-ray reflectivity data using a conventional power diffractometer, *Thin Solid Films* **230**, 99-101 (1993).

[30] M. Yasaka, X-ray thin-film measurement techniques, *The Rigaku J.* **26**, 1 (2010).

[31] B. D. Cullity, *Elements of X-ray Diffraction* (Addison-Wesly Publishing Company Inc., Reading MA, 1956).

[32] G. K. Pálsson, A. R. Rennie, and B. Hjörvarsson, Examination of the reliability of x-ray techniques for determining hydrogen-induced volume changes, *Phys. Rev. B* **78**, 104118 (2008).

[33] F. Tao, M. E. Grass, Y. Zhang, D. R. Butcher, J. R. Renzas, Z. Liu, J. Y. Chung, B. S. Mun, M. Salmeron, and G. A. Somorjai, Reaction-driven restructuring of Rh-Pd and Pt-Pd core-shell nanoparticles, *Science* **322**, 932 (2008).

[34] M. Salmeron, L. Brewer, and G. A. Somorjai, The structure and stability of surface platinum oxide and of oxides of other noble metals, *Surf. Sci.* **112**, 207 (1981).

[35] E. Yang, D. E. Laughlin, and J.-G. Zhu, Correction of order parameter calculations for FePt perpendicular thin films, *IEEE Trans. Magn.* **48**, 7 (2012).

[36] H. K. Kim, H. You, R. P. Chiarello, H. L. M. Chang, T. J. Zhang, and D. J. Lam, Finite-size effect on the first-order metal-insulator transition in VO_2 films grown by metal-organic chemical-vapor deposition, *Phys. Rev. B* **47**, 12900 (1993).

[37] D. Kande, S. Pisana, D. Weller, D. E. Laughlin, and J.-G. Zhu, Enhanced B2 Ordering of FeRh Thin Films Using B2 NiAl Underlayers, *IEEE Trans. Magn.* **47**, 3296 (2011).

[38] A. Hillion, A. Cavallin, S. Vlaic, A. Tamion, F. Tournus, G. Khadra, J. Dreiser, C. Piamonteze, F. Nolting, S. Rusponi, *et al.*, Low temperature ferromagnetism in chemically ordered FeRh nanocrystals, *Phys. Rev. Lett.* **110**, 087207 (2013).

[39] J. W. Koo, S. Mitani, T. T. Sasaki, H. Sukegawa, Z. C. Wen, T. Ohkubo, T. Niizeki, K. Inomata, and K. Hono, Large perpendicular magnetic anisotropy at Fe/MgO interface, *Appl. Phys. Lett.* **103**, 192401 (2013).

[40] L. Benito, T. A. Moore, and C. H. Marrows (unpublished).

[41] S. P. Bennett, A. T. Wong, A. Glavic, A. Herklotz, C. Urban, I. Valmianski, M. D. Biegalski, H. M. Christen, T. Z. Ward, and V. Lauter, Giant controllable magnetization changes induced by structural phase transitions in a metamagnetic artificial multiferroic, *Sci. Rep.* **6**, 22708 (2016).

[42] D. Odkhuu, Magnetization reversal of giant perpendicular magnetic anisotropy at the magnetic-phase transition in FeRh films on MgO, *Phys. Rev. B* **93**, 064412 (2016).

[43] S. I. Csiszar, M. W. Haverkort, Z. Hu, A. Tanaka, H. H. Hsieh, H.-J. Lin, C. T. Chen, T. Hibma, and L. H. Tjeng, Controlling orbital moment and spin orientation in CoO layers by strain, *Phys. Rev. Lett.* **95**, 187205 (2005).

[44] J. Lee, G. Lauhoff, M. Tselepi, S. Hope, P. Rosenbusch, J. A. C. Bland, H. A. Dürr, G. van der Laan, J. Ph. Schilléand, and J. A. D. Matthew, Evidence for a strain-induced variation of the magnetic moment in epitaxial Cu/Ni/Cu/Si(100) structures, *Phys. Rev. B* **55**, 15103 (1997).

[45] L. Benito, K. Dumesnil, and R. C. C. Ward, Direct evidence of the anisotropy of magnetization in rare-earth metals and rare-earth/Fe_2 alloys, *Phys. Rev. B* **90**, 054407 (2014).

[46] C. Baldasseroni, C. Bordel, A. X. Gray, A. M. Kaiser, F. Kronast, J. Herrero-Albillos, C. M. Schneider, C. S. Fadley, and F. Hellman, Temperature-driven nucleation of ferromagnetic domains in FeRh thin films, *Appl. Phys. Lett.* **100**, 262401 (2012).

[47] M. Morita, T. Ohmi, E. Hasegawa, M. Kawakami, and M. Ohwada, Growth of native oxide on a silicon surface, *J. Appl. Phys.* **68**, 1272 (1990).

[48] A. Ruíz-Baltazar, R. Esparza, G. Rosas, and R. Pérez, Effect of the Surfactant on the Growth and Oxidation of Iron Nanoparticles, *J. Nanomater.* **2015**, 240948 (2015).

[49] J. Evertsson, F. Bertram, F. Zhang, L. Rullik, L. R. Merte, M. Shipilin, M. Soldemo, S. Ahmadi, N. Vinogradov, F. Carlà, J. Weissenrieder, M. Göthelid, J. Pan, A. Mikkelsen, J.-

O. Nilsson, and E. Lundgren, The thickness of native oxides on aluminum alloys and single crystals, *Appl. Surf. Sci.* **349**, 826 (2015).

[50] J. A. Thornton, Influence of apparatus geometry and deposition conditions on the structure and topography of thick sputtered coatings, *J. Vac. Sci. Technol.*, **11**, 666 (1974).

[51] J. A. Thornton, The microstructure of sputter-deposited coatings, *J. Vac. Sci. Technol. A*, **4**, 3059 (1986).

[52] K. Oura, V. G. Lifshits, A. Saranin, A. V. Zotov, M. Katayama (eds.), *Surface Science: An Introduction* (Springer-Verlag Berlin Heidelberg, Berlin 2003).

[53] M. Copel, M. C. Reuter, E. Kaxiras, and R. M. Tromp, Surfactants in epitaxial growth, *Phys. Rev. Lett.* **63**, 632 (1989).

[54] S. H. Overbury, P. A. Bertrand, and G. A. Samorjai, The surface composition of binary systems, *Chem. Rev.* **75**, 547 (1975).

[55] L. Z. Mezey and J. Giber, The surface free energies of solid chemical elements: Calculation from internal free enthalpies of atomization, *Jpn. J. Appl. Phys.* **21**, 1569 (1982).

[56] M. W. Thompson, The energy spectrum of ejected atoms during the high energy sputtering of gold, *Phil. Mag.* **18**, 377 (1968).

[57] G. K. Wehner and G. S. Anderson, in L. I. Maissel and R. Glang (eds.), *Handbook of Thin Film Technology* (McGraw-Hill, New York, 1970, p. 3-1).

[58] B. Chapman, *Glow discharge Processes* (Wiley New York, 1980, p. 200-234).

[59] R. V. Stuart, *Vacuum Technology, Thin Films and Sputtering* (Academic Press, New York 1983, p.91-131).

[60] R. Fürth, On the equation of state for solids, *Proc. R. Soc. London Ser. A* **183**, 87 (1944).

[61] D. W. Hoffman and J. A. Thornton, Internal stresses in sputtered chromium, *Thin Solid Films* **40**, 355 (1977).

[62] A. Bessaudou, J. Machet, and C. Weissmantel, Transport of evaporated material through support gas in conjunction with ion plating: I, *Thin Solid Films* **149**, 225 (1987).

[63] A. Bessaudou, J. Machet, and C. Weissmantel, Transport of evaporated material through support gas in conjunction with ion plating: II, *Thin Solid Films* **149**, 237 (1987).

[64] J. L. Vossen and W. Kern (Eds.), *Thin Film Processes II* (Academic Press, 1991).

[65] D. L. Smith, *Thin Film Deposition* (McGraw-Hill Inc., New York 1995, p. 23).

[66] https://www.pfeiffer-vacuum.com/en/know-how/introduction-to-vacuum-technology/fundamentals/mean-free-path/

[67] F. M. D'Heurle and J. M. E. Harper, Note on the origin of intrinsic stresses in films deposited via evaporation and sputtering, *Thin Solid Films* **171**, 81 (1989).

[68] L. J. Swartzendruber, The Fe-Rh (Iron-Rhodium) System, *Bull. Alloy Phase Diagr.* **5**, 456 (1984).

[69] J. E. Greene, Epitaxial crystal growth by sputter deposition: Applications to semiconductors. Part I, *Crit. Rev. Solid State* **11**, 47 (1983).

[70] S. F. Edwards, and D. R. Wilkinson, The surface statistics of a granular aggregate, *Proc. R. Soc. London Ser. A* **381**, 17 (1982).

[71] M. Kardar, G. Parisi, and Y.-C. Zhang, Dynamic scaling of growing interfaces, *Phys. Rev. Lett.* **56**, 889 (1986).

[72] Z-W. Lai and S. Das Sarma, Kinetic growth with surface relaxation: Continuum versus atomistic models, *Phys. Rev. Lett.* **66**, 2348 (1991).

[73] Z. Zhang, J. Detch, and H. Metiu, Surface roughness in thin-film growth: The effect of mass transport between layers, *Phys. Rev. B* **48**, 4972 (1993).